Dynamic behavior of the melt pool at severe accident conditions

Andrej Horvat and Ivo Kljenak
Reactor Engineering Division
"Jožef Stefan" Institute
Ljubljana, Slovenia
andrej.horvat@ijs.si, ivo.kljenak@ijs.si

Jure Marn
Faculty of Mechanical Engineering
University of Maribor
Maribor, Slovenia
jure.marn@uni-mb.si

KEYWORDS

severe accident, core melting, lower plenum, heat transfer, natural convection

ABSTRACT

Prediction of thermal loads on lower plenum walls after core melting and relocation during severe accident conditions requires knowledge about the core melt behavior, especially the circulation pattern. To analyze the heat transfer dynamics on the lower plenum walls, two-dimensional numerical simulations of a fluid flow with internal heat generation were performed for Rayleigh numbers 10^6, 10^7, 10^8, 10^9, 10^{11} and 10^{13} at Prandtl number 0.8. For subgrid motion modeling, the Large Eddy Simulation (LES) Smagorinsky model was implemented. Time and boundary-averaged Nusselt numbers were calculated. Results show that differences between minimum, average and maximum Nusselt number increase in exponential manner when the Rayleigh number is increased beyond 10^8. Probability densities of Nusselt number were also calculated to realistically assess unsteady thermal loads. The calculated probability density functions indicate that time-average Nusselt numbers usually do not coincide with most probable values. The study also discloses the appearance of multiple Nusselt number probability peaks.

1. INTRODUCTION

Inadequate or prolonged absence of nuclear reactor core cooling may cause core melting to occur. The reactor core melt relocates, flowing downward towards the reactor pressure vessel lower plenum where it accumulates. In the past few years, the issue of lower plenum coolability during the described severe accident scenario has received much attention. According to the state-of-the-art knowledge about this issue, the reactor

vessel integrity would be maintained. However, this has not yet been proven with either a full-scale experiment or an adequate numerical simulation.

Prediction of thermal loads on lower plenum walls requires knowledge about the fluid behavior, especially about the circulation pattern, which is, due to high temperature gradients, mainly governed by buoyancy forces in the melt pool. For these reasons the present work is focused on natural convection in the core melt.

Previous experimental and numerical works from various authors often presented only the mean values of Nusselt number at the lower plenum boundaries without describing the uncertainties of obtained results. Such information about thermal load could be misleading. Namely, at higher Rayleigh numbers ($Ra > 10^8$), the fluid circulation patterns become unsteady, which leads first to local and then to global turbulent motion, so that mean values of Nusselt number do not coincide with most probable values. This suggests that single-value calculations of heat transfer values in the lower plenum should be supplemented with probability distributions or at least with extreme (minimum and maximum) values.

2. MATHEMATICAL MODEL

2.1 Transport equations

The basic assumption in the present work was to consider the melt as an incompressible fluid with internal heat generation. Following this assumption, the melt behavior was described with mass, momentum and energy equations:

$$\nabla \cdot \vec{v} = 0 \ , \tag{1}$$

$$\frac{\partial \vec{v}}{\partial t} + \nabla \cdot (\vec{v} \otimes \vec{v}) = -\frac{1}{\rho} \nabla p + \nabla \cdot \underline{\underline{\tau}} - \beta \Delta T \, \vec{g} \ , \tag{2}$$

$$\frac{\partial T}{\partial t} + \nabla \cdot (\vec{v} T) = \frac{\lambda}{c_p \rho} \nabla^2 T + \frac{I}{c_p \rho} \ . \tag{3}$$

To reduce the number of free parameters in the calculations and to simplify the comparison of results, Eqs. (1), (2) and (3) were transformed into dimensionless form using Boussinesq' s approximation to include buoyancy forces:

$$\nabla \cdot \vec{v} = 0 \ , \tag{4}$$

$$\frac{\partial \vec{v}}{\partial t} + \nabla \cdot (\vec{v} \otimes \vec{v}) = -\nabla p + \Pr \left(\nabla \cdot \underline{\underline{\tau}} \right) - \operatorname{Ra} \Pr T \frac{\vec{g}}{|\vec{g}|} \ , \tag{5}$$

$$\frac{\partial T}{\partial t} + \nabla \cdot (\vec{v} T) = \nabla^2 T + 1 \ . \tag{6}$$

A complete description of dimensionless variables may be found in Horvat (1998).

2.2 Turbulence modeling

At high Rayleigh numbers (Ra>10^8) at which simulations were performed, time-aperiodic behavior occurs. When the Rayleigh number is further increased (Ra>10^9) local turbulent motion appear, reducing the local scale of fluid motion.

To properly take into account the subgrid motion of the fluid, the Large-Eddy Simulation (LES) Smagorinsky model was implemented, with a modification to capture also the buoyancy forces due to temperature gradients (as presented by Eidson, 1985). After applying the Large-Eddy Simulation concept of spatial filtering, Eqs. (4), (5) and (6) are written as:

$$\nabla \cdot \bar{\vec{v}} = 0 \quad , \tag{7}$$

$$\frac{\partial \bar{\vec{v}}}{\partial t} + \nabla \cdot \left(\bar{\vec{v}} \otimes \bar{\vec{v}}\right) = -\nabla \bar{p} + \Pr\left(\nabla^2 \bar{\vec{v}}\right) - \mathrm{Ra}\Pr\bar{T}\frac{\vec{g}}{|\vec{g}|} + \nabla \cdot \left(\nu_{sgd} 2\underline{\bar{S}}\right) \quad , \tag{8}$$

$$\frac{\partial \bar{T}}{\partial t} + \nabla \cdot \left(\bar{\vec{v}}\,\bar{T}\right) = \nabla^2 \bar{T} + 1 + \nabla \cdot \left(\upsilon_{sgd} \nabla \bar{T}\right) \quad , \tag{9}$$

where the overbar indicates filtered values. The non-linear convection term of subgrid velocities in the momentum equation acts as a stress term with artificial subgrid viscosity, which is defined according to Eidson (1985) as:

$$\nu_{sgd} = \left(C_s \Delta x\right)^2 \left(2\underline{S} : \underline{S} + \frac{\mathrm{Ra}\,\mathrm{Pr}}{\mathrm{Pr}_{sgd}}\left(\nabla\bar{T} \cdot \frac{\vec{g}}{|\vec{g}|}\right)\right)^{1/2} \quad . \tag{10}$$

The first term in Eq. (10) represents stress forces while the second term represents buoyancy. Similarly, the non-linear convection term of subgrid velocities and temperature in the energy equation can be replaced with diffusive flux using the subgrid thermal diffusity defined as a linear function of subgrid viscosity:

$$\upsilon_{sgd} = \frac{\nu_{sgd}}{\mathrm{Pr}_{sgd}} \quad . \tag{11}$$

The presented Smagorinsky model is too dissipative in the vicinity of the walls. To reduce the near wall dissipation, the subgrid viscosity was multiplied by the van Driest dumping functions (Patankar and Spalding, 1970).

2.3 Geometrical considerations

Although experimental and numerical results for semi-circular and elliptical cavities are already available (Theofanous et al., 1997), a square cavity was used to simplify calculations at high Rayleigh numbers. The comparison of experimental results from natural convection cases in rectangular and spherical cavities reveals the similarity

of heat transfer processes in both geometries. Moreover, it is safe to assume that the maximum Nusselt number is similar for rectangular and spherical cavities of similar dimensions. The maximum Nusselt number occurs in the upper corners of the cavities. Larger discrepancies between heat transfer in rectangular and spherical cavities occur only in the lower parts (Asfia and Dhir, 1996; Nourgaliev et al., 1997).

Experimental and numerical results presented by Dinh and Nourgaliev (1997) and Nourgaliev et al. (1997) suggest that the fluid pattern is basically two-dimensional. A two-dimensional model should thus be adequate for the simulation of considered phenomena.

2.4 Initial and boundary conditions

At the simulation beginning, the fluid was considered at rest with an isothermal temperature field.

For the momentum equation, no-slip boundary conditions at all boundaries of the rectangular cavity were prescribed. To represent the solidification and melting processes at the walls of the lower plenum, isothermal boundary conditions at all boundaries were prescribed for the energy equation.

3. NUMERICAL METHODS

3.1 Numerical mesh

The transport Eqs. (7), (8) and (9) were discretized according to a finite volume method using 128 x 128 numerical cells. A staggered arrangement for grid points was applied.

The high Rayleigh numbers and modest number of grid points used in the presented calculations required local mesh refinement. This was necessary for accurate simulation of the viscous sublayer behavior at the boundaries of the simulation domain. In the x-direction, the numerical mesh was refined according to Eq. (12):

$$\Delta x_i = \frac{L_x}{n_x - 1}\left(\varphi + (1-\varphi)Sin^2\left(\pi \frac{i}{n_x}\right)\right), \tag{12}$$

whereas in the y-direction, it was refined according to Eq. (13):

$$\Delta y_j = \frac{L_y}{n_y - 1}\left(\varphi + (1-\varphi)Sin^2\left(\pi \frac{j}{n_y}\right)\right), \tag{13}$$

where the parameter φ was set equal to 0.2.

3.2 Discretisation techniques

Spatial discretisation of transport Eqs. (7), (8) and (9) followed the way of central-symmetric discretisation on a staggered grid (Harlow and Welsh, 1965).

Time integration was independent from spatial discretization. For the energy Eq. (9), the second-order accurate explicit Adams-Bashforth scheme was implemented:

$$\frac{\overline{T}^{n+1} - \overline{T}^n}{\Delta t^n} = RHS^{n+1/2} \quad, \tag{14}$$

$$RHS^{n+1/2} = RHS^n + 0.5\Delta t^n \frac{\left(RHS^n - RHS^{n-1}\right)}{\Delta t^{n-1}} \quad. \tag{15}$$

In the case of the momentum Eq. (8), a combination of the Adams-Bashforth scheme and the projection method was used.

The parabolic pressure equation, which arises from combining Eqs. (7) and (8) to satisfy the mass conservation principle, was solved with the Conjugate Gradient method (Ferziger and Perić, 1996).

3.3 Stability

Time step stability restrictions for time integration were taken from explicit central symmetric scheme for convection-diffusion equation. The diffusion stability condition implemented in the numerical scheme is formulated as:

$$\Delta t \left(\nu + \nu_{sgd}\right)_{j,i} \left(\frac{1}{\Delta x_i^2} + \frac{1}{\Delta y_j^2}\right) = 0.25 \tag{16}$$

and the combined convection-diffusion stability condition as:

$$\Delta t \left(\frac{v_x^2 + v_y^2}{\nu + \nu_{sgd}}\right)_{j,i} = 2.0 \quad. \tag{17}$$

The largest time step which satisfied both conditions, (16) and (17), was used for time marching.

4. RESULTS

Simulations were performed for Rayleigh numbers 10^6, 10^7, 10^8, 10^9, 10^{11} and 10^{13}. An extrapolation with a 3rd-order polynomial was used to obtain time-averaged Nusselt numbers for Rayleigh number 10^{15}, which corresponds to realistic accident conditions. The Prandtl number was 0.8 in all cases. Figure. 1 presents a sample of calculated unsteady flow field (Ra=10^9).
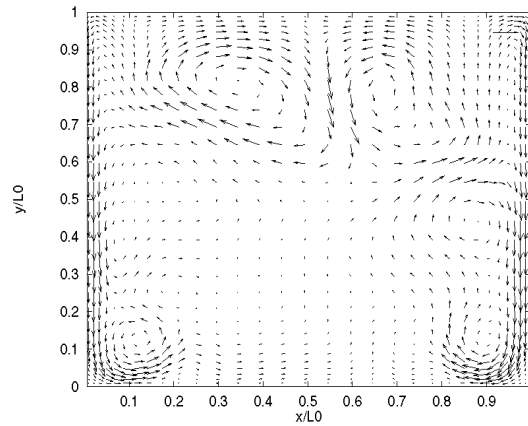
Fig. 1   An example of instantaneous flow field at Ra=10^9.

4.1 Time and local-averaged Nusselt numbers

First, time and boundary-averaged Nusselt numbers were calculated. Rayleigh-Nusselt number dependencies are presented in $\log_{10}$-$\log_{10}$ diagrams. Minimum and maximum Nusselt numbers are plotted along with the averaged Nusselt number. Calculated Rayleigh-Nusselt number dependencies are also compared with experimental results of other authors. On Figs. 2-4, K&G indicates results of Kulacki and Goldstein (1972), whareas S&R indicates results of Steinberner and Reineke (1978).

On Fig. 2, the Rayleigh-Nusselt number dependencies for the bottom boundary are presented. Calculated values of Nusselt number agree well with experimental results at lower Rayleigh numbers. Differences increase when the Rayleigh number exceeds the value 10^{10}. Similar overestimated results can also be observed in the work of other authors (e.g. Nourgaliev et al., 1997) which conducted numerical simulations of natural convection in a melt pool.
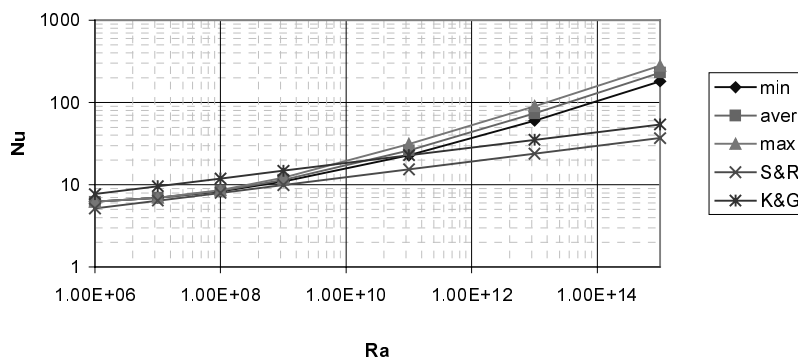
Fig. 2   Rayleigh number vs. Nusselt number for the bottom boundary.

When the average Nusselt numbers are compared with minimum and maximum Nusselt numbers reached, observable differences first occur at Rayleigh number 10^8. At this point, a steady-state fluid circulation cannot be reached. The system experiences a

(6)

bifurcation behavior of heat transfer variables. Figure 2 shows that differences between minimum, average and maximum Nusselt numbers are slightly increasing in the $\log_{10}$-$\log_{10}$ diagram with increasing Rayleigh number. Although this trend is very slow in the $\log_{10}$-$\log_{10}$ diagram, it means that differences increase in exponential manner in the linear Rayleigh-Nusselt number diagram.
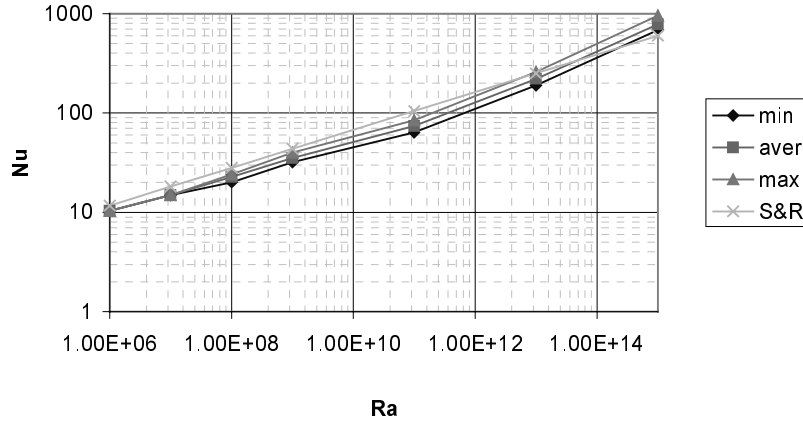

Fig. 3   Rayleigh number vs. Nusselt number for the side boundary.

       On Fig. 3, the Rayleigh-Nusselt number dependencies for the side walls are presented. The calculated results show good agreement with experimental results of Steinberner & Reineke (1978) for a rectangular cavity.

       Again, we cannot confirm the linear dependence between Rayleigh and Nusselt numbers in the $\log_{10}$-$\log_{10}$ diagram. The differences occur first at Rayleigh number 10^8, where a steady state cannot be established. Between Rayleigh numbers 10^9 and 10^{11} the slower increase in Nusselt numbers coincides with the flow transition from laminar to turbulent regime. Above Rayleigh number 10^{11} the Rayleigh-Nusselt number dependences are basically linear in the $\log_{10}$-$\log_{10}$ diagram.
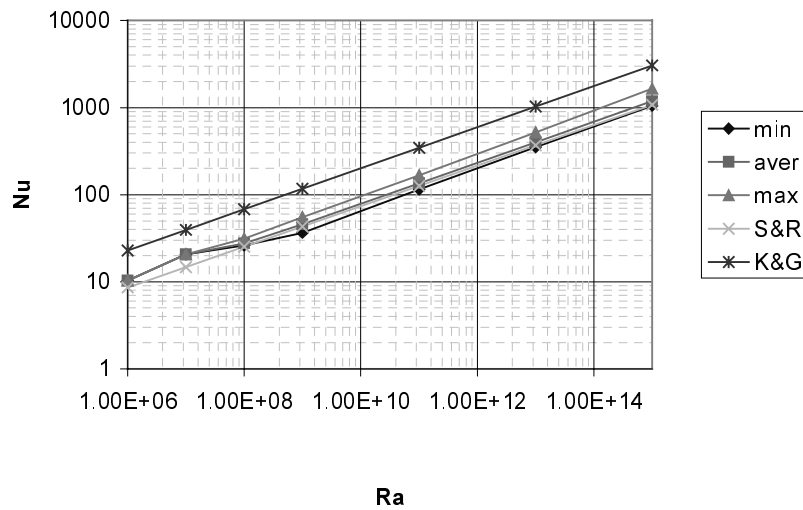

Fig. 4   Rayleigh number vs. Nusselt number for the upper boundary.

On Fig. 4, the Rayleigh-Nusselt number dependencies for the upper wall are presented. The Nusselt numbers there are higher than on the bottom boundary and comparable to those on the side boundaries. The calculated results show again good agreement with experimental results of Steinberner & Reineke (1978) and are lower that those obtained by Kulacki & Goldstein (1972) for a fluid layer.

The differences between minimum, average and maximum Nusselt numbers appear first at Rayleigh number 10^8 on the bottom and side walls. The transition to turbulence is not as distinctive as on the side walls due to the nature of Rayleigh-Taylor instabilities at the upper boundary. These instabilities, which produce "jets" of cold fluid from the upper boundary towards the center of the simulation domain and appear immediately after Rayleigh number exceeds 10^8, cause random-like behavior of the fluid flow at the upper boundary. The higher the Rayleigh numbers, the stronger are the jets of cold fluid. The described random-like behavior of the fluid flow at the upper boundary also causes a wider range between minimum and maximum Nusselt numbers than on the bottom and side walls.

4.2 Time-averaged Nusselt number distributions

Along with the differences between minimum, average and maximum Nusselt numbers, the probability densities of Nusselt numbers are also important. Namely, to realistically determine the threat to lower plenum integrity, the probability of thermal loads has to be known. From this point on, the present paper describes an attempt to realistically assess time-dependent values of heat transfer on the boundaries. The presented values of Nusselt number (Figs. 5-19) show the complexity of boundary layer behavior at high Rayleigh numbers.

At Rayleigh numbers 10^6 and 10^7 the fluid circulation is stable, forming two counter-rotating vortices. The Nusselt number is low at the bottom (Fig. 5) and increases towards the upper boundary of the simulation domain (Fig. 6). A local maximum is reached in the upper corner on the sidewalls. Similar values of Nusselt number may also be observed on parts of the upper boundary (Fig. 7).
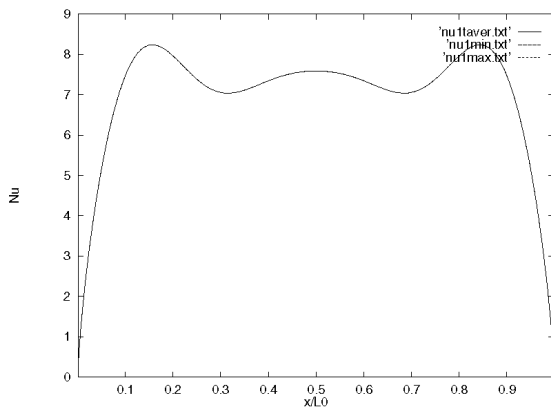

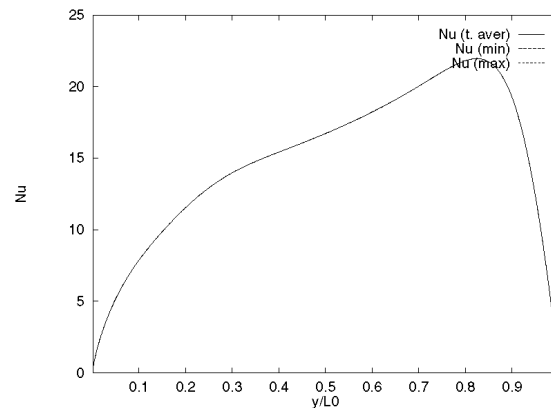**Fig. 5** Nusselt number at the bottom boundary, $Ra = 10^7$, $Pr = 0.8$ **Fig. 6** Nusselt number at the side boundary, $Ra = 10^7$, $Pr = 0.8$

At Rayleigh number 10^7, Rayleigh-Taylor instabilities, which are the result of intensive cooling of the fluid at the top, cause a jet of cold fluid from the upper boundary

towards the center of the simulation domain to appear. The jet produces two additional and stable vortices. The consequences of the described process appear on Fig. 7 as a deep valley in the Nusselt number curve.

A similar process occurs also in the lower corners of the simulation domain where it causes local increases in Nusselt number (Fig. 5). The phenomenon is not limited only to the rectangular geometry but can be also observed in hemispherical and elliptical geometries as presented by Nourgaliev et al. (1997).
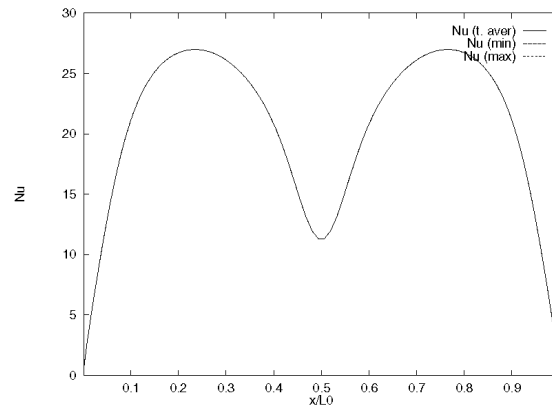
Fig. 7 Nusselt number at the upper
boundary, Ra $= 10^7$, Pr $= 0.8$

At Rayleigh number 10^8, the fluid circulation does not reach a steady state after the initial thermal transient. This results in time-dependence of the Nusselt number, where the minimum, average and maximum Nusselt number can be distinguished as shown on Figs. 8, 10 and 12. The differences between minimum, average and maximum local Nusselt numbers are larger on the side and upper boundaries where the Nusselt numbers are also higher than on the bottom boundary.

The two peaks on the bottom Nusselt number curve (Fig. 8) show that the additional vortices caused by downward flow at the side walls are stronger than at Rayleigh number 10^7. The large Nusselt number differences on Fig. 10 also indicates the appearance of Kelvin-Helmholz instabilities between upward flow powered by internal heat generation and downward flow at cold side walls. On the upper boundary (Fig. 12) the Nusselt number inclination reveals a stable jet of cold fluid towards the center of the simulation domain, which does not change its position nor strength in time. On both sides the large differences between minimum, average and maximum Nusselt number show additional locations of the Rayleigh-Taylor instabilities which result in the appearance of time-dependent jets.
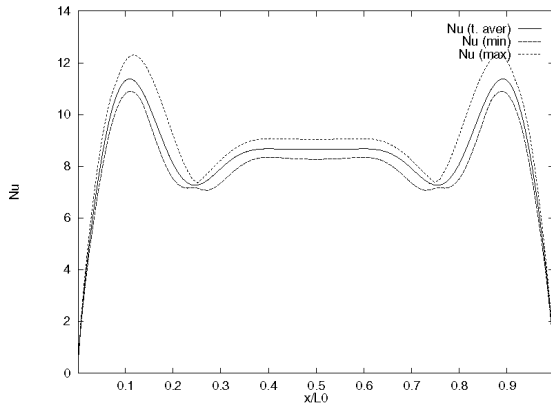
(9)

Fig. 8 Nusselt number at the bottom
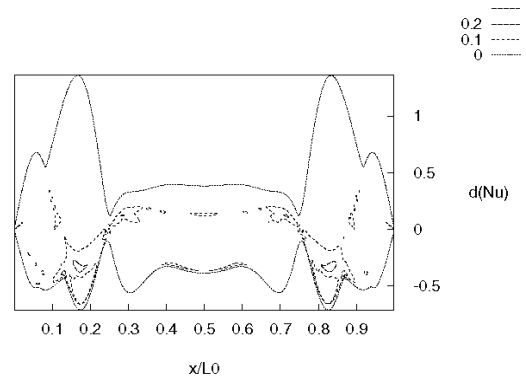boundary, $Ra = 10^8$, $Pr = 0.8$

Fig. 9 Probability density at the bottom
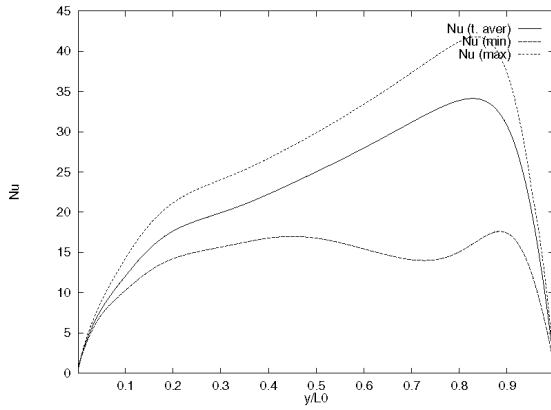boundary, $Ra = 10^8$, $Pr = 0.8$

Fig. 10 Nusselt number at the side
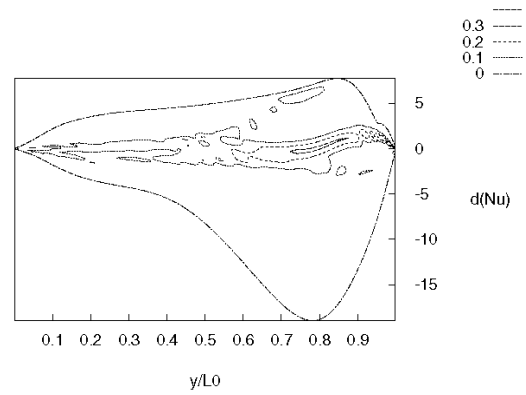boundary, $Ra = 10^8$, $Pr = 0.8$

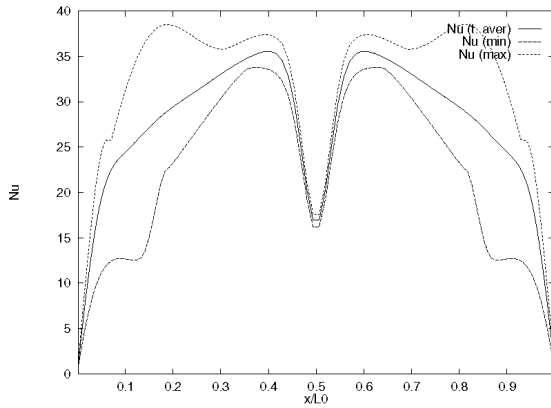**Fig. 11** Probability density at the side
boundary, $Ra = 10^8$, $Pr = 0.8$

Fig. 12 Nusselt number at the upper
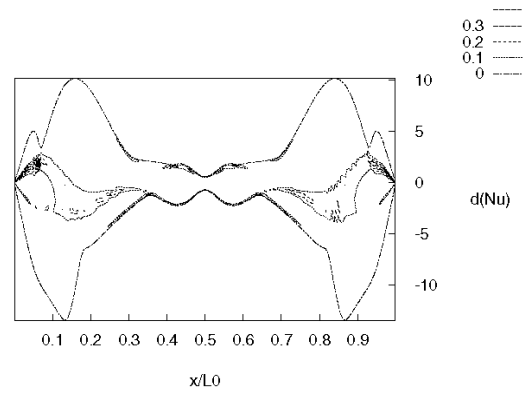boundary, $Ra = 10^8$, $Pr = 0.8$

Fig. 13 Probability density at the upper
boundary, $Ra = 10^8$, $Pr = 0.8$

(10)

On Figs. 9, 11 and 13 the contours of Nusselt number probability densities (observed from "above") at Rayleigh number 10^8 and Prandtl number 0.8 are presented. The diagrams' abscissa represents the coordinate on the boundary whereas the ordinate represents the Nusselt number difference :

$$d(\text{Nu}) = Nu^n - Nu_{aver} \tag{19}$$

To obtain probability density functions, approximately 2000 calculated local Nusselt numbers were distributed in 20 classes between the minimum and the maximum Nusselt number. The number of samples in each class was than divided by the total number of samples.

The probability densities of local Nusselt number significantly differ from the Gauss function. The contours on Figs. 9, 11 and 13 reveal that the average Nusselt number usually does not coincide with the most probable value. Figure 9 shows that the probability density function of the Nusselt number for the bottom boundary is very narrow with local peaks, which alternate around the average Nusselt number value. On the side boundaries (Fig. 11) the function is wider with compactly arranged density peaks around average Nusselt values. Figure 13, where the probability density function for upper wall is presented, reveals that there is also a possibility of two probability peaks for the Nusselt number distribution. This typically indicates a bifurcation behavior where two flow patterns are equally possible, alternating through time from one to another.

On Figs. 14, 16 and 18 the local Nusselt numbers for the bottom boundary are presented to show heat transfer dynamics when the Rayleigh number is increased. When the Rayleigh number exceeds 10^9, the local Nusselt number distributions on the boundaries become asymmetric due to time-dependent vortices which appear at the boundaries.

On Fig. 14 two additional peaks on maximum Nusselt number curve are present which are not evident on Fig. 8. This is the result of two additional vortices, which appear rarely and without changing the average of Nusselt number. When the Rayleigh number is further increased to 10^{11} (Fig. 16) the appearance of the vortices on the bottom boundary is not limited to the lower corners of the simulation domain. The whole bottom boundary is exposed to the mixing of cold downward flow and hot buoyancy flow. Although the fluid structures appear as almost stochastic, the general shape of average Nusselt number curve, which was first observed at lower Rayleigh numbers, is preserved. On Fig. 18 the local Nusselt numbers on the bottom boundary at Rayleigh number 10^{13} are presented. The Nusselt number distributions exhibit the stochastic behavior of the fluid flow. Local peaks in Nusselt number function indicate modest size of fluid structures, which is characteristic for turbulent flow regime. The weak similarity between minimum, average and maximum Nusselt number functions also confirms the time-dependence of fluid structures and the unsteadiness of the heat transfer on the bottom boundary.
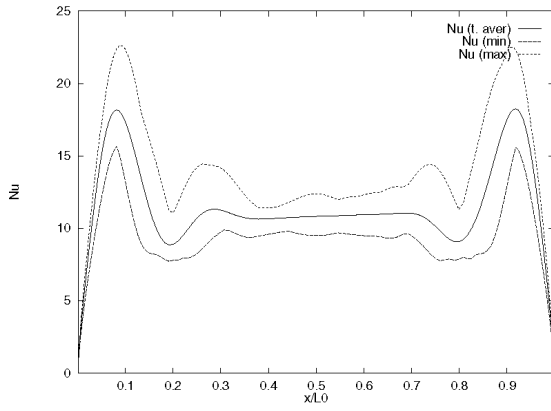
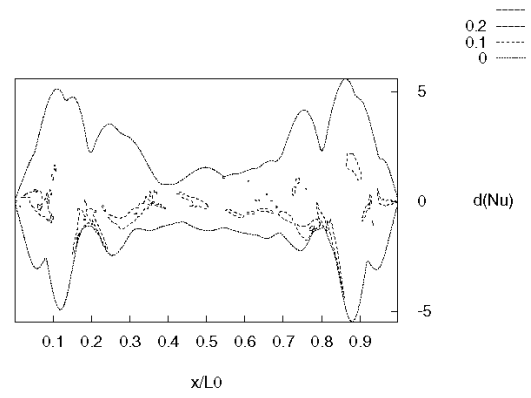**Fig. 14** Nusselt number at the bottom boundary, $Ra = 10^9$, $Pr = 0.8$

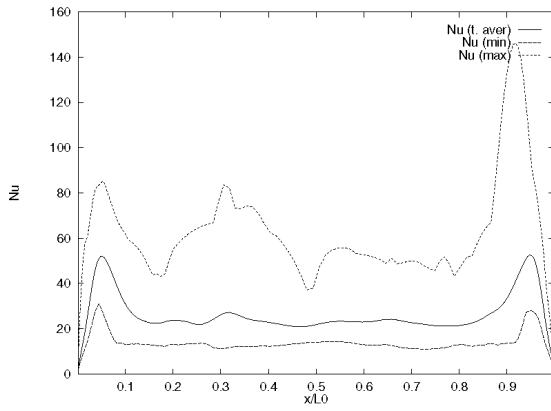**Fig. 15** Probability density at the bottom boundary, $Ra = 10^9$, $Pr = 0.8$

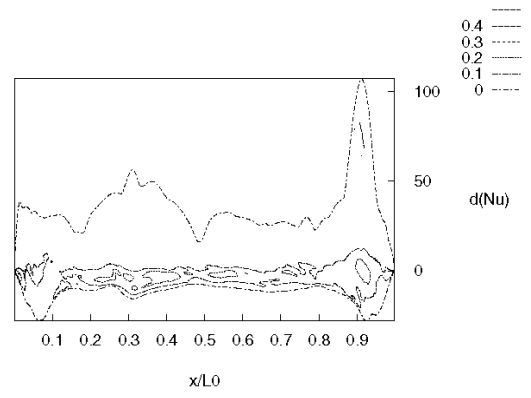**Fig. 16** Nusselt number at the bottom boundary, $Ra = 10^{11}$, $Pr = 0.8$

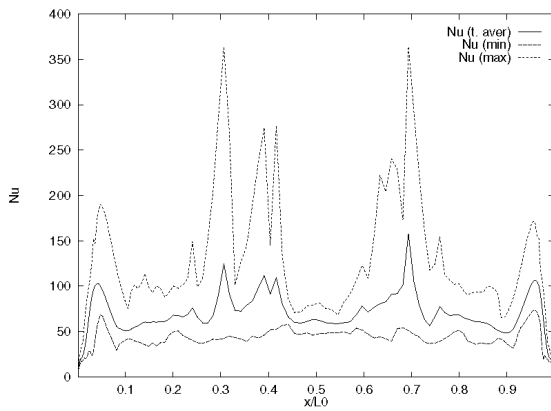**Fig. 17** Probability density at the bottom boundary, $Ra = 10^{11}$, $Pr = 0.8$

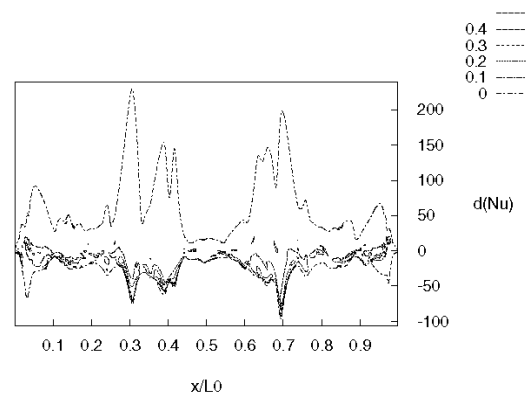**Fig. 18** Nusselt number at the bottom boundary, $Ra = 10^{13}$, $Pr = 0.8$

Fig. 19 Probability density at the bottom boundary, $Ra = 10^{13}$, $Pr = 0.8$

(12)

The probability densities of local Nusselt number differ from the Gauss function and also from the probability densities at lower Rayleigh numbers. On the bottom and upper boundaries the symmetry is no longer preserved (Fig. 15). As it is evident from Figs. 15, 17 and 19, the differences between minimum and maximum Nusselt numbers increase. With increasing Rayleigh number the probability density functions are also becoming more flat. This is the result of stochastic fluid motion where the probability of vortex appearance is similar at different locations.

Although the probability densities of local Nusselt number are more flat as in the case of Rayleigh number 10^8, the multiple peaks of probability density functions are higher and more compactly organized around average Nusselt number (Figs. 17 and 19). The reason for such qualitative changes in probability density functions is in the fundamental differences between bifurcational flow (Figs. 8-13) and turbulent flow (Figs. 14 -19).

Similar observations could also be made for the side and upper boundaries of the simulation domain.

5. CONCLUSIONS

Two-dimensional numerical simulations of a fluid flow with internal heat generation in a rectangular cavity at Rayleigh numbers from 10^6 to 10^{13} were performed to investigate heat transfer dynamics in the reactor pressure vessel lower plenum at severe accident conditions. To capture the fluid subgrid motion, the Large-Eddy Simulation (LES) Smagorinsky model was applied.

The first purpose of the numerical experiments was to examine the Nusselt number behavior on the boundaries of the simulation domain at different Rayleigh numbers. Local and time-averaged Nusselt numbers were calculated and compared with experimental results of other authors, showing satisfactory agreement. These simulation results were then extrapolated to Rayleigh number 10^{15}, which corresponds to realistic accident conditions.

Dynamics of Nusselt number were also analyzed. The results reveal that differences between minimum, average and maximum Nusselt numbers over the boundaries of the simulation domain increase with increasing Rayleigh number. The calculated Nusselt number probability density functions indicate that time-averaged Nusselt numbers usually do not coincide with most probable values. The study also discloses the appearance of multiple Nusselt number probability peaks. Therefore, the results of this work suggest that the usually presented average values of Nusselt number should be supplemented with probability density functions to realistically assess thermal loads on the lower plenum walls.

NOMENCLATURE

C_s Smagorinsky constant
c_p specific heat
g gravity
I volumetric heat generation
L length of simulation domain
Nu   Nusselt number, $(\partial T / \partial x_i)\, L / (T_w - T_{aver})$
p pressure
Pr   Prandtl number ν / υ
Ra   Rayleigh number, $\left(|\vec{g}| \beta I L^5\right) / (\nu \lambda \upsilon)$
RHS right-hand-side of convection-diffusion equation
$\underline{S}$ deformation velocity tensor, $S_{j,i} = 0.5(\partial v_x / \partial y + \partial v_y / \partial x)$
T temperature
t time
v velocity
β temperature dilatation
λ thermal conductivity
ρ mass density
φ mesh generation parameter
ν kinematic viscosity
υ thermal diffusivity
$\underline{\tau}$ stress tensor

Subscripts

$aver$ average
i,j indices
n number of grid points
sgd subgrid or turbulent variable
w wall
x horizontal direction
y vertical direction

Superscript

n number of iteration

REFERENCES

Asfia, F.J., Dhir, V.K., 1996. An experimental study of natural convection in a volumetrically heated spherical pool bounded on top with a rigid wall, *Nucl. Eng. Design* **163**, pp. 333-348.

Decker, W.J., Numerical studies of bifurcations and chaos in natural convection, Ph.D. Thesis, Virginia University, 1996.

Dinh, T.N., Nourgaliev, R.R., 1997. Turbulence modeling for large volumetrically heated liquid pools, *Nucl. Eng. Design* **169**, pp. 131-151.

Eidson, T.M., 1985. Numerical simulation of the turbulent Rayleigh-Benard problem using subgrid modelling, *J. Fluid. Mech.*, **158**, pp. 245-268.

Ferziger, J.H., Perić, M., 1996. *Computational Methods for Fluid Mechanics*, Springer Verlag, Berlin, pp. 101-106.

Harlow, F.H., Welch, J.E., 1965, Numerical calculation of time-dependent viscous incompressible flow of fluid with free surface, *Phys of Fluids* **8**, pp. 2182-2189.

Hindmarsh, A.C., Gresho, P.M., Griffiths, D.F., 1984. The stability of explicit Euler time-integration for certain finite difference approximations of the multi-dimensional advection-diffusion equation, *Int. J. Num. Meth. Fluids* **4**, pp. 853-897.

Horvat, A., Modeling of natural convection phenomena in nuclear reactor core melt, M.Sc. Thesis, Faculty of Mathematics and Physics, University of Ljubljana, 1998, *http://www2.ijs.si/~ahorvat*.

Kulacki, F.A., Goldstein, R.J., 1972. Thermal convection in a horizontal fluid layer with uniform volumetric energy sources, *J. Fluid Mech.* **83**, pp. 375-395.

Nourgaliev, R.R., Dinh, T. N., Sehgal, B.R., 1997. Effect of fluid Prandtl number on heat transfer characteristics in internally heated liquid pools with Rayleigh number up to 10^{12}, *Nucl. Eng. Design* **169**, pp. 165-184.

Patankar, S.V., Spalding, D.B., 1970. Heat and Mass Transfer in Boundary Layers, 2nd Edition, Intertext Books, London, p. 21.

Steinberner, U., Reineke, H.H., 1978. Turbulent buoyancy convection heat transfer with internal heat sources, *Proceedings of 6th Int. Heat Transfer Conference*, Vol. II, Toronto, Canada, pp. 305-310.

Theofanous, T.G., Liu, C., Additon, S., Angelini, S., Kymäläinen, O., Salmassi, T., 1997. In-vessel coolability and retention of a core melt, *Nucl. Eng. Design* **169**, pp. 1-49.